15. Y. Manassen, R. J. Hamers, J. E. Demuth, A. J. Castellano Jr., *Phys. Rev. Lett.* **62**, 2531–2534 (1989).
16. Y. Manassen, I. Mukhopadhyay, N. Rao, *Phys. Rev. B* **61**, 16223–16228 (2000).
17. C. Durkan, M. E. Welland, *Appl. Phys. Lett.* **80**, 458 (2002).
18. A. V. Balatsky, M. Nishijima, Y. Manassen, *Adv. Phys.* **61**, 117–152 (2012).
19. S. Müllegger *et al.*, *Phys. Rev. Lett.* **113**, 133001 (2014).
20. Supplementary materials are available on *Science* Online.
21. S. Baumann *et al.*, Interplay between orbital magnetic moment and crystal field symmetry: Fe atoms on MgO. Available at http://arxiv.org/abs/1506.07807 (2015).
22. B. Chilian *et al.*, *Phys. Rev. B* **84**, 212401 (2011).
23. I. G. Rau *et al.*, *Science* **344**, 988–992 (2014).
24. A. Kiel, W. B. Mims, *Phys. Rev.* **153**, 378–385 (1967).
25. R. E. George, J. P. Edwards, A. Ardavan, *Phys. Rev. Lett.* **110**, 027601 (2013).
26. F. Dolde *et al.*, *Nat. Phys.* **7**, 459–463 (2011).
27. A. Laucht *et al.*, *Sci. Adv.* **1**, e1500022 (2015).
28. S. Loth, M. Etzkorn, C. P. Lutz, D. M. Eigler, A. J. Heinrich, *Science* **329**, 1628–1630 (2010).

ACKNOWLEDGMENTS

We thank B. Melior for expert technical assistance and B. A. Jones, S. Gangopadhyay, and R. M. Macfarlane for fruitful discussions. We gratefully acknowledge financial support from the Office of Naval Research. W.P. thanks the Natural Sciences and Engineering Research Council of Canada for fellowship support.

SUPPLEMENTARY MATERIALS

www.sciencemag.org/content/350/6259/417/suppl/DC1
Supplementary Text
Figs. S1 to S13
Table S1
References (*29*, *30*)

27 June 2015; accepted 18 September 2015
10.1126/science.aac8703

QUANTUM OPTICS

Direct sampling of electric-field vacuum fluctuations

C. Riek, D. V. Seletskiy, A. S. Moskalenko, J. F. Schmidt, P. Krauspe, S. Eckart, S. Eggert, G. Burkard, A. Leitenstorfer*

The ground state of quantum systems is characterized by zero-point motion. This motion, in the form of vacuum fluctuations, is generally considered to be an elusive phenomenon that manifests itself only indirectly. Here, we report direct detection of the vacuum fluctuations of electromagnetic radiation in free space. The ground-state electric-field variance is inversely proportional to the four-dimensional space-time volume, which we sampled electro-optically with tightly focused laser pulses lasting a few femtoseconds. Subcycle temporal readout and nonlinear coupling far from resonance provide signals from purely virtual photons without amplification. Our findings enable an extreme time-domain approach to quantum physics, with nondestructive access to the quantum state of light. Operating at multiterahertz frequencies, such techniques might also allow time-resolved studies of intrinsic fluctuations of elementary excitations in condensed matter.

Vacuum fluctuations give rise to a variety of phenomena, from spontaneous photon emission (*1*, *2*) and the Lamb shift (*3*) via the Casimir force (*4*) to cosmological perturbations (*5*, *6*). Representing the ground state, the quantum vacuum does not possess intensity. However, finite noise amplitudes of electric and magnetic fields should exist because of Heisenberg's uncertainty principle. These fluctuations are best explained by analogy with a harmonic oscillator of mass m, resonance angular frequency Ω, and total energy

$$H_{\mathrm{HO}} = \frac{1}{2}\left(\frac{p^2}{m} + m\Omega^2 x^2\right) = \frac{m}{2}\left(\dot{x}^2 + \Omega^2 x^2\right) \qquad (1)$$

Quantization results in noncommuting operators for momentum p and displacement x. The Gaussian wave function of the ground state exhibits a root-mean-square (RMS) standard deviation of $\Delta x = (\hbar/2\Omega m)^{1/2}$ (*7*, *8*), where $\hbar$ is the reduced Planck constant. The total energy of a radiation field of wavevector $\mathbf{k}$ in free space, with electric and magnetic amplitudes E and B (respectively), and vector potential $\mathbf{A}$ in the Coulomb gauge is (*9*)

$$H_{\mathrm{RF}} = \frac{\varepsilon_0 V}{2}\left(E^2 + c^2 B^2\right) = \frac{\varepsilon_0 V}{2}\left(\dot{A}^2 + c^2 |\mathbf{k} \times \mathbf{A}|^2\right) \qquad (2)$$

Considering one polarization direction and the transverse character of electromagnetic waves, Eq. 1 maps onto Eq. 2 by replacing x with A (amplitude of vector potential $\mathbf{A}$), m with $\varepsilon_0 V$ (ε_0, vacuum permittivity; V, spatial volume), and Ω with $ck \equiv \Omega$ (c, speed of light; $k = |\mathbf{k}|$). Instead of x and p, an uncertainty product now links E and B or the amplitudes and phases of E, B, or A. An RMS amplitude of vacuum fluctuations $\Delta A = (\hbar/2\Omega\varepsilon_0 V)^{1/2}$ results. In contrast to the mechanical case where Δx is known, understanding ΔA is less straightforward: Outside any cavities, there are no obvious boundaries that define a normalization volume V. This situation raises the question of whether direct measurement of the vacuum field amplitude in free space is physically meaningful and feasible.

The quantum properties of light (*10*) are typically analyzed either by photon correlation (*11*–*14*), homodyning (*15*–*18*), or hybrid measurements (*19*). In those approaches, information is averaged over multiple cycles, and accessing the vacuum state requires amplification. Femtosecond studies still rely on pulse envelopes that vary slowly relative to the carrier frequency (*20*–*23*). In our work, we directly probed the vacuum noise of the electric field on a subcycle time scale using laser pulses lasting a few femtoseconds. In ultrabroadband electro-optic sampling (*24*–*27*), a horizontally polarized electric-field waveform (red in Fig. 1A) propagates through an electro-optic crystal (EOX), inducing a change Δn of the linear refractive index n_0 that is proportional to its local amplitude E_{THz} (Fig. 1A and fig. S1). The geometry is adjusted so that a new index ellipsoid emerges under 45° to the polarization of E_{THz}, with $n_{y'}$ and $n_{x'} = n_0 \pm \Delta n$. An ultrashort optical probe pulse at a much higher carrier frequency ν_{p} (green in Fig. 1A; intensity, I_{p}; electric field, E_{p}) copropagates with E_{THz} at a variable delay time t_{d}. The envelope of I_{p} has to be on the order of half a cycle of light at the highest frequencies $\Omega/2\pi$ of E_{THz} that are detected. We used probe pulses as short as t_{p} = 5.8 fs, corresponding to less than 1.5 optical cycles at ν_{p} = 255 THz (fig. S2). Upon passage through the EOX, the x' and y' components of E_{p} acquire a relative phase delay proportional to Δn and $E_{\mathrm{THz}}(t_{\mathrm{d}})$. The final polarization state of the probe is analyzed with ellipsometry. The differential photocurrent $\Delta I/I$ is proportional to the electric field $E_{\mathrm{THz}}(t_{\mathrm{d}})$. We used a radio-frequency lock-in amplifier (RFLA) for readout.

We adjusted for optimal conditions to measure the vacuum signal by studying classical multiterahertz transients, which were synchronized to the probe (*8*). In Fig. 1B, $\Delta I/I$ is plotted in red against delay time t_{d}. Figure 1C shows the amplitude spectrum (red) and phase deviations (blue) within ±π, corroborating calculations (*8*) of an effective sampling bandwidth of $\Delta\nu = \Delta\Omega/2\pi$ = 66 THz (figs. S3 and S4) around a center frequency of $\nu_{\mathrm{c}} = \Omega_{\mathrm{c}}/2\pi$ = 67.5 THz (free-space wavelength λ_{c} = 4.4 μm). The electric-field amplitude $\bar{E}_{\mathrm{THz}}(t_{\mathrm{d}})$ is calibrated using (*28*–*30*)

$$\frac{\Delta I}{I} = \sin\left(\frac{2\pi\,\nu_{\mathrm{p}}\, r_{41}\, n_0^3\, l\, |R(\Omega_{\mathrm{c}})|}{c}\ \bar{E}_{\mathrm{THz}}\right) \approx \frac{2\pi\,\nu_{\mathrm{p}}\, r_{41}\, n_0^3\, l\, |R(\Omega_{\mathrm{c}})|}{c}\ \bar{E}_{\mathrm{THz}} \qquad (3)$$

r_{41} denotes the electro-optic coefficient, and l is the thickness of the EOX. The amplitude response $|R(\Omega_{\mathrm{c}})|$ includes the pulse duration of the probe and velocity matching to the multiterahertz phase (*8*). The classical field transient in Fig. 1B was

Department of Physics and Center for Applied Photonics, University of Konstanz, D-78457 Konstanz, Germany.
***Corresponding author. E-mail: alfred.leitenstorfer@uni-konstanz.de**

sampled with a signal-to-noise ratio better than 10^3 at a RFLA detection bandwidth set to 94 Hz. From the confocal amplitude trace and cross section, we estimated a mean photon number below 900 per pulse. This result proves the capability of our approach to characterize ultrabroadband coherent wave packets containing less than 10^{-3} photons, on average, within 1 s.

But can we directly access the ground state Φ_0 of the radiation field? With the pump branch switched off, electro-optic phase shifts might still be caused by vacuum fluctuations copropagating with the probe. This effect should lead to a statistical distribution of the signal around the average of $\langle \bar{E}_{vac} \rangle = 0$. The ground-state expectation value of the squared operator for the electric field in free space (*31*) yields the RMS amplitude

$$\Delta\bar{E}_{vac} = \sqrt{\left\langle \Phi_0 \left| \sum_{\Omega=\Omega_c-\Delta\Omega/2}^{\Omega_c+\Delta\Omega/2} \frac{-\hbar\Omega}{2\varepsilon_0 V}\left(\hat{a}_\Omega - \hat{a}_\Omega^\dagger\right)^2 \right| \Phi_0 \right\rangle}$$

$$= \sqrt{\left\langle \Phi_0 \left| \sum_{\Omega=\Omega_c-\Delta\Omega/2}^{\Omega_c+\Delta\Omega/2} \frac{\hbar\Omega}{2\varepsilon_0 V}\left(-\hat{a}_\Omega^2 + \hat{a}_\Omega\hat{a}_\Omega^\dagger + \hat{a}_\Omega^\dagger\hat{a}_\Omega - \hat{a}_\Omega^{\dagger 2}\right) \right| \Phi_0 \right\rangle}$$

$$= \sqrt{\sum_{\nu=\nu_c-\Delta\nu/2}^{\nu_c+\Delta\nu/2} \frac{h\nu}{2\varepsilon_0 V}} \qquad (4)$$

$\hat{a}_\Omega$ and $\hat{a}_\Omega^\dagger$ are the operators for annihilation and creation of a photon with angular frequency Ω, respectively (ν, frequency; h, Planck constant).

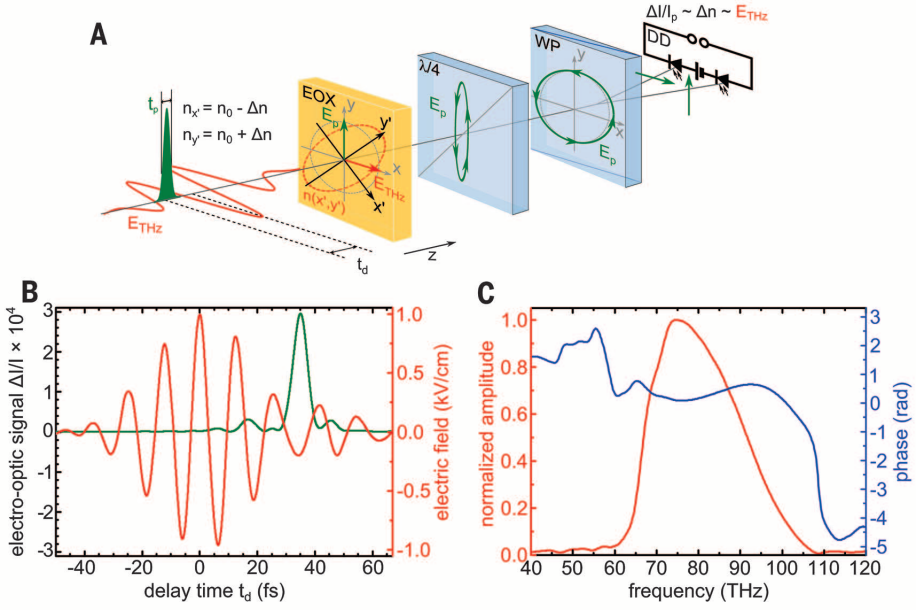

Fig. 1. Our experimental principle, with a demonstration of ultrahigh bandwidth and sensitivity. (**A**) Scheme of electro-optic sampling of an electric-field waveform (red) by an ultrafast probe pulse (green), consisting of an EOX, a quarter-wave plate (λ/4), a Wollaston polarizer (WP), and a differential photocurrent detector (DD). (**B**) Classical electro-optic signal $\Delta I/I$ and corresponding electric-field amplitude versus delay time t_d (red line). The intensity envelope of the 5.8-fs probe pulse is shown in arbitrary units for comparison (green line). (**C**) Spectral multiterahertz amplitude (red) and phase (blue) obtained by Fourier transform.

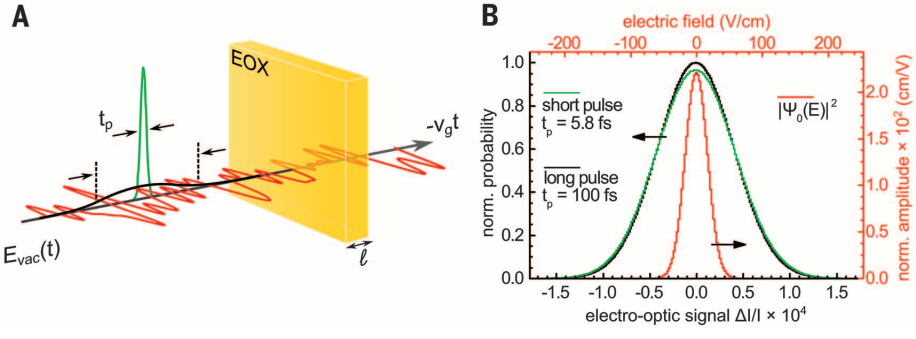

Fig. 2. Studying vacuum fluctuations via statistic readout and longitudinal modification of the probed space-time volume. (**A**) Diagram showing longitudinal expansion of the probe volume: Stretching the sampling pulse from 5.8 fs (green) to 100 fs (black) causes temporal averaging over the vacuum field (red), leading to a reduction of the detected noise amplitude (t_p, pulse duration; v_g, group velocity). (**B**) Normalized counting probability as a function of electro-optic readout by the short pulse (green) and long pulse (stretched to 100 fs; black). The deconvolved wave function $|\Psi_0|^2$ of the electric-field ground state is shown in red.

Because of the commutation relation $[\hat{a}_\Omega, \hat{a}_\Omega^\dagger] = 1$, only $\hat{a}_\Omega\hat{a}_\Omega^\dagger$ provides a nonvanishing contribution. Summing frequencies over our finite sensitivity interval ensures convergence of Eq. 4. The lateral extension of the volume V is now identified with the effective cross section A_{eff}, defined by the Gaussian intensity profile of the near-infrared probe beam inside the EOX. Theoretical modeling based on Laguerre-Gaussian modes (*30*) yields $A_{eff} = w_0{}^2\pi$, where w_0 is the probe spot radius (*8*). Because $V = A_{eff}L$, only the length L remains to be determined. Periodic boundary conditions are applicable when the EOX is short relative to the Rayleigh range of the multiterahertz transverse mode, resulting in a density of free-space modes L/c. Summing over all longitudinal modes within a bandwidth of $\Delta\nu$ eliminates L, and we obtain

$$\Delta\bar{E}_{vac} = \sqrt{\frac{h\nu_c\Delta\nu}{2\pi c n_0 \varepsilon_0 w_0^2}} = 20.2\,\frac{\mathrm{V}}{\mathrm{cm}} \qquad (5)$$

A factor of $n_0{}^{-1/2}$ accounts for dielectric screening inside the EOX (*8*). Thus, the vacuum amplitude is maximized when averaging over a minimal space-time volume, determined in the transverse directions by w_0 = 4.25 μm (fig. S5). The longitudinal cross section $cn_0/(\nu_c\Delta\nu)$ is defined by the Fourier transform of $R(\Omega)$, containing the intensity envelope of the 5.8-fs probe pulse and phase-matching conditions within the EOX (*8*).

Are such fluctuations discernible on top of the shot noise due to the Poissonian photon statistics of the coherent probe? An average number of $N_p = 5 \times 10^8$ photons detected per pulse causes a relative RMS shot-noise current of $\Delta I_{SN}/I = N_p{}^{-1/2}$. With Eq. 3, we obtain the noise-equivalent field

$$\Delta E_{SN} = \frac{c}{2\pi\nu_p r_{41} n_0^3 l \sqrt{N_p}|R(\Omega_c)|} = 65.0\,\frac{\mathrm{V}}{\mathrm{cm}} \qquad (6)$$

Because the shot noise of the near-infrared probe, which is centered around ν_p, and the vacuum fluctuations at multiterahertz frequencies Ω are uncorrelated with each other and lack spectral overlap, the two contributions add up in quadrature. Therefore, the RMS width of the total detected noise distribution is expected to rise by a factor of

$$\frac{\Delta E_{total}}{\Delta E_{SN}} = \frac{\sqrt{\Delta E_{SN}^2 + \Delta\bar{E}_{vac}^2}}{\Delta E_{SN}} = 1.047 \qquad (7)$$

corresponding to a 4.7% increase, due to the multiterahertz vacuum noise.

To experimentally access the statistics of the quantum vacuum, we extended the RFLA bandwidth to 1.6 MHz and sampled the probability distribution of the electric field $P(E_{total})$ every 5 μs. The contribution of the multiterahertz vacuum can be modified to discriminate against the shot-noise baseline by longitudinal or transverse expansion of the probed space-time volume (Eq. 5). In the first approach, we decreased ν_c and $\Delta\nu$ by chirping the probe pulse to 100 fs (fig. S3), via

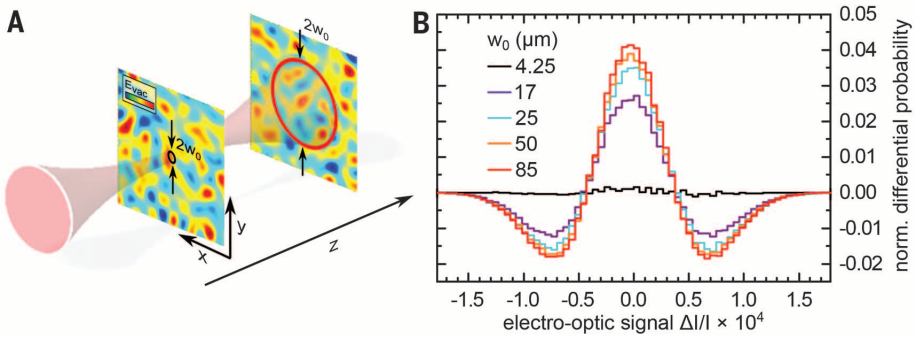

Fig. 3. Detection by transverse expansion of the space-time segment. (**A**) Sketch showing the lateral increase of the sampling cross section, which leads to averaging over noise patterns within the circled areas. (**B**) Differential histograms obtained by subtracting the result for the confocal detector position with w_0 = 4.25 μm from the results for positions with the beam diameter at 4.25 μm (black), 17 μm (purple), 25 μm (cyan), 50 μm (orange), and 85 μm (red).

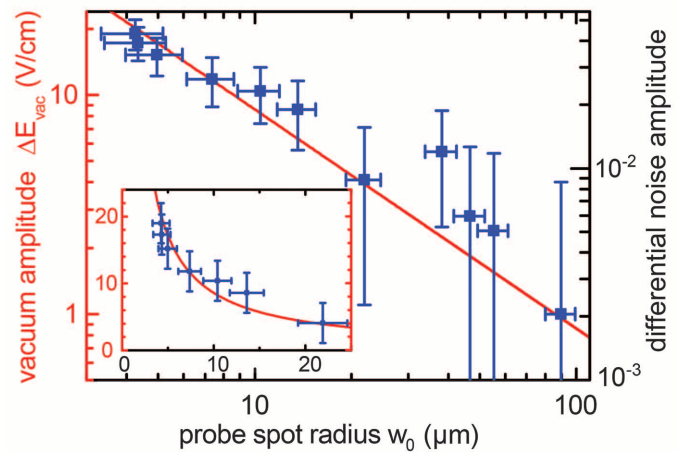

Fig. 4. Dependence of the vacuum amplitude on transverse extension of the probed space-time volume. Relative excess noise of electro-optic signal Δ*I*/*I* (right vertical axis) and RMS vacuum amplitude ΔE_{vac} (left vertical axis) versus probe radius w_0 (blue squares). Red lines represent a theoretical assessment based on Eq. 5.

translation of an SF10 prism in the compressor stage (Fig. 2A). A distinct reduction in peak counts around $P(E_{total} = 0)$ is observed when comparing the probability distribution obtained with the 5.8-fs probe (green in Fig. 2B) to the measurement with a stretched pulse (black). Also, the probabilities in the wings of the distribution including the multiterahertz vacuum (5.8-fs probe) are consistently higher than the corresponding values in the stretched-pulse distribution. The total change of the normalized noise amplitude amounts to 4%, in good agreement with the theoretical considerations underlying Eqs. 5 to 7. The red histogram in Fig. 2B emerges from a deconvolution algorithm that searches for the best link between distributions of $P(E_{total})$ obtained with and without vacuum noise. This result directly mirrors the ground-state wave function $|\Psi_0(E)|^2$ of the electromagnetic field in the polarization plane and space-time volume that we probed. From $|\Psi_0(E)|^2$, a RMS standard deviation of $\Delta\tilde{E}_{vac}$ = 18 V/cm is obtained, in good agreement with the theoretical prediction of 20.2 V/cm in Eq. 5.

In the transverse option, we kept the short pulse duration and expanded the probe radius w_0 by translating the EOX out of the confocal plane (Fig. 3A). Averaging over a larger cross section causes a decrease in fluctuation amplitude, which is projected onto the transverse mode of the gate. The effect of progressive narrowing is emphasized with differential probabilities obtained by subtracting a distribution at w_0 = 4.25 μm from $P(E_{total})$ sampled at increasing spot radii (Fig. 3B). When all original histograms are normalized, the maximum change in probability $\Delta P(E_{total} = 0)$ of 0.04 ≡ 4% directly corresponds to the difference between the relative noise amplitudes measured with and without multiterahertz vacuum fluctuations, in quantitative agreement with Eq. 7. The dependence of the vacuum RMS amplitude on the transverse extension of the probed space-time volume is shown in Fig. 4. The normalized increase of total noise, measured with respect to bare shot noise (right vertical axis), is plotted against the probe spot radius w_0 (blue squares). Conversion to the vacuum electric amplitude ΔE_{vac} (left vertical axis) has been carried out analogously to $|\Psi_0(E)|^2$ in Fig. 2B. The functional dependence expected from Eq. 5 is shown as a red line. The inset in Fig. 4 illustrates the data recorded at low beam cross sections on a linear scale to highlight the hyperbolic increase of vacuum fluctuations for the smaller space-time volumes that we probed.

In our study, we directly monitored vacuum fluctuations without amplifying them. The only effective part $\sum_{\Omega>0} \hat{a}_\Omega \hat{a}_\Omega^+$ of the operator that extracts the variance of the field in Eq. 4 indicates that vacuum fluctuations correspond to photons, which spontaneously arise and vanish in the ground state Φ_0. Time-energy uncertainty demands that virtual excitations have a limited lifetime on the order of their oscillation cycle (*32*). The subcycle temporal resolution provided by the ultrashort probe ensures that we can directly detect effects originating from purely virtual photons. Phase-matched copropagation of the vacuum field and probe inside the EOX maximizes those signals. But does this measurement influence the quantum vacuum at all? Based on the electro-optic change of the refractive index $\Delta n_p \sim r_{41} E_{THz}$, the local multiterahertz field imprints a phase shift onto the ultrashort probe, which we detected. Because sum- and difference-frequency mixing occur simultaneously in this process (*29*), it requires no net transfer of energy, momentum, or angular momentum, and it even avoids modulation of the refractive index at frequencies $\Omega/2\pi << \nu_p$. Our second-order nonlinear element operates far from resonance. Virtual driving of the transitions avoids problems with decoherence, distinguishing our experiment from detection approaches in quantum optics or circuit quantum electrodynamics in which resonant two-level systems are involved (*33*). In consequence, our approach may be used to study the multiterahertz ground state while imposing negligible influence on it. Back-action might arise only in third order: The nonlinear refractive index n_2 generates a local anomaly of phase velocity copropagating with the intensity envelope of the probe, because $\Delta n_\Omega \sim n_2 |E_p|^2$. When $N_p/w_0^2 t_p$ suffices to induce phase shifts of the multiterahertz field during passage through the EOX, depletion of the vacuum amplitude in the sampled space-time volume and enhanced fluctuations in an adjacent interval are expected.

REFERENCES AND NOTES

1. W. Vogel, D.-G. Welsch, *Quantum Optics* (Wiley-VCH, Weinheim, Germany, ed. 3, 2006).
2. D. F. Walls, G. J. Milburn, *Quantum Optics* (Springer-Verlag, Berlin, ed. 2, 2008).
3. W. E. Lamb Jr., R. C. Retherford, *Phys. Rev.* **72**, 241–243 (1947).
4. H. Casimir, *Proc. Kon. Ned. Akad. Wetensch. B* **51**, 793–795 (1948).
5. E. P. Tryon, *Nature* **246**, 396–397 (1973).
6. V. F. Mukhanov, H. A. Feldman, R. H. Brandenberger, *Phys. Rep.* **215**, 203–333 (1992).
7. F. Schwabl, *Quantum Mechanics* (Springer-Verlag, Berlin, ed. 4, 2007).
8. Materials and methods are available as supplementary materials on *Science* Online.
9. J. D. Jackson, *Classical Electrodynamics* (Wiley, New York, ed. 3, 1999).
10. I. A. Walmsley, *Science* **348**, 525–530 (2015).
11. R. Hanbury Brown, R. Q. Twiss, *Nature* **177**, 27–29 (1956).
12. H. J. Kimble, M. Dagenais, L. Mandel, *Phys. Rev. Lett.* **39**, 691–695 (1977).
13. P. Michler *et al.*, *Nature* **406**, 968–970 (2000).
14. B. Lounis, W. E. Moerner, *Nature* **407**, 491–493 (2000).

15. R. E. Slusher, L. W. Hollberg, B. Yurke, J. C. Mertz, J. F. Valley, *Phys. Rev. Lett.* **55**, 2409–2412 (1985).
16. L.-A. Wu, H. J. Kimble, J. L. Hall, H. Wu, *Phys. Rev. Lett.* **57**, 2520–2523 (1986).
17. D. T. Smithey, M. Beck, M. G. Raymer, A. Faridani, *Phys. Rev. Lett.* **70**, 1244–1247 (1993).
18. A. I. Lvovsky *et al.*, *Phys. Rev. Lett.* **87**, 050402 (2001).
19. N. B. Grosse, T. Symul, M. Stobińska, T. C. Ralph, P. K. Lam, *Phys. Rev. Lett.* **98**, 153603 (2007).
20. A. M. Fox, J. J. Baumberg, M. Dabbicco, B. Huttner, J. F. Ryan, *Phys. Rev. Lett.* **74**, 1728–1731 (1995).
21. M. E. Anderson, M. Beck, M. G. Raymer, J. D. Bierlein, *Opt. Lett.* **20**, 620–622 (1995).
22. C. Silberhorn *et al.*, *Phys. Rev. Lett.* **86**, 4267–4270 (2001).
23. P. J. Mosley *et al.*, *Phys. Rev. Lett.* **100**, 133601 (2008).
24. Q. Wu, X.-C. Zhang, *Appl. Phys. Lett.* **71**, 1285–1286 (1997).
25. A. Leitenstorfer, S. Hunsche, J. Shah, M. C. Nuss, W. H. Knox, *Appl. Phys. Lett.* **74**, 1516–1518 (1999).
26. K. Liu, J. Z. Xu, X.-C. Zhang, *Appl. Phys. Lett.* **85**, 863–865 (2004).
27. C. Kübler, R. Huber, S. Tübel, A. Leitenstorfer, *Appl. Phys. Lett.* **85**, 3360–3362 (2004).
28. S. Namba, *J. Opt. Soc. Am.* **51**, 76–79 (1961).
29. G. Gallot, D. Grischkowsky, *J. Opt. Soc. Am. B* **16**, 1204–1212 (1999).
30. A. S. Moskalenko, C. Riek, D. V. Seletskiy, G. Burkard, A. Leitenstorfer, http://arxiv.org/abs/1508.06953 (2015).
31. R. Loudon, P. L. Knight, *J. Mod. Opt.* **34**, 709–759 (1987).
32. C. Fürst, A. Leitenstorfer, A. Laubereau, R. Zimmermann, *Phys. Rev. Lett.* **78**, 3733–3736 (1997).
33. A. A. Clerk, M. H. Devoret, S. M. Girvin, F. Marquardt, R. J. Schoelkopf, *Rev. Mod. Phys.* **82**, 1155–1208 (2010).

ACKNOWLEDGMENTS

Support by the European Research Council (Advanced Grant 290876 "UltraPhase"), by Deutsche Forschungsgemeinschaft (SFB767), and by NSF via a postdoctoral fellowship for D.V.S. (award no. 1160764) is gratefully acknowledged.

SUPPLEMENTARY MATERIALS

www.sciencemag.org/content/350/6259/420/suppl/DC1
Materials and Methods
Figs. S1 to S5
References (*34*–*40*)

8 July 2015; accepted 16 September 2015
Published online 1 October 2015
10.1126/science.aac9788

ASTEROSEISMOLOGY

Asteroseismology can reveal strong internal magnetic fields in red giant stars

Jim Fuller,[1,2]*† Matteo Cantiello,[2]*† Dennis Stello,[3,4] Rafael A. Garcia,[5] Lars Bildsten[2,6]

Internal stellar magnetic fields are inaccessible to direct observations, and little is known about their amplitude, geometry, and evolution. We demonstrate that strong magnetic fields in the cores of red giant stars can be identified with asteroseismology. The fields can manifest themselves via depressed dipole stellar oscillation modes, arising from a magnetic greenhouse effect that scatters and traps oscillation-mode energy within the core of the star. The Kepler satellite has observed a few dozen red giants with depressed dipole modes, which we interpret as stars with strongly magnetized cores. We find that field strengths larger than ~10^5 gauss may produce the observed depression, and in one case we infer a minimum core field strength of ≈10^7 gauss.

Despite rapid progress in the discovery and characterization of magnetic fields at the surfaces of stars, very little is known about internal stellar magnetic fields. This has prevented the development of a coherent picture of stellar magnetism and the evolution of magnetic fields within stellar interiors.

After exhausting hydrogen in their cores, most main sequence stars evolve up the red giant branch (RGB). During this phase, the stellar structure is characterized by an expanding convective envelope and a contracting radiative core. Acoustic waves (p modes) in the envelope can couple to gravity waves (g modes) in the core (*1*). Consequently, nonradial stellar oscillation modes become mixed modes that probe both the envelope (the p-mode cavity) and the core (the g-mode cavity), as illustrated in Fig. 1. Mixed modes (*2*) have made it possible to distinguish between hydrogen- and helium-burning red giants (*3*, *4*) and have been used to measure the rotation rate of red giant cores (*5*, *6*).

A group of red giants with depressed dipole modes were identified using observations from the Kepler satellite [(*7*), see also Fig. 2]. These stars show normal radial modes (spherical harmonic degree $\ell = 0$) but exhibit dipole ($\ell = 1$) modes whose amplitude is much lower than usual. Until now, the suppression mechanism was unknown (*8*). Below, we demonstrate that dipole mode suppression may result from strong magnetic fields within the cores of these red giants.

Red giant oscillation modes are standing waves that are driven by stochastic energy input from turbulent near-surface convection (*9*, *10*). Waves excited near the stellar surface propagate downward as acoustic waves until their angular frequency ω is less than the local Lamb frequency for waves of angular degree ℓ; i.e., until $\omega = L_\ell = \sqrt{\ell(\ell+1)}\,v_s/r$, where v_s is the local sound speed and r is the radial coordinate. At this boundary, part of the wave flux is reflected, and part of it tunnels into the core.

The wave resumes propagating inward as a gravity wave in the radiative core where $\omega < N$, where N is the local buoyancy frequency. In normal red giants, wave energy that tunnels into the core eventually tunnels back out to produce the observed oscillation modes. We show here that suppressed modes can be explained if wave energy leaking into the core never returns back to the stellar envelope.

The degree of wave transmission between the core and envelope is determined by the tunneling integral through the intervening evanescent zone. The transmission coefficient is

$$T \sim \left(\frac{r_1}{r_2}\right)^{\sqrt{\ell(\ell+1)}} \quad (1)$$

where r_1 and r_2 are the lower and upper boundaries of the evanescent zone, respectively. The fraction of wave energy transmitted through the evanescent zone is T^2. For waves of the same frequency, larger values of ℓ have larger values of r_2, thus Eq. 1 demonstrates that high ℓ waves have much smaller transmission coefficients through the evanescent zone.

The visibility of stellar oscillations depends on the interplay between driving and damping of the modes (*10*, *11*). To estimate the reduced mode visibility due to energy loss in the core, we assume that all mode energy that leaks into the g-mode cavity is completely lost. The mode then loses a fraction T^2 of its energy in a time 2 t_{cross}, where t_{cross} is the wave crossing time of the acoustic cavity. Due to the larger energy loss rate, the mode has less energy E_{ac} within the acoustic cavity and produces a smaller luminosity fluctuation V at the stellar surface, whose amplitude scales as $V^2 E_{ac}$. We show (*12*) that the ratio of visibility between a suppressed mode V_{sup} and its normal counterpart V_{norm} is

$$\frac{V_{sup}^2}{V_{norm}^2} = [1 + \Delta\nu\ \tau\ T^2]^{-1} \quad (2)$$

where $\Delta\nu \simeq (2\ t_{cross})^{-1}$ (*13*) is the large frequency separation between acoustic overtone modes, and τ is the damping time of a radial mode with similar frequency. We evaluate T^2 from our stellar models using Eq. 6, whereas $\tau \approx 5$ to 10 days (*10*, *14*–*16*) for stars ascending the RGB.

[1]TAPIR, Walter Burke Institute for Theoretical Physics, Mailcode 350-17 California Institute of Technology, Pasadena, CA 91125, USA. [2]Kavli Institute for Theoretical Physics, University of California, Santa Barbara, CA 93106, USA. [3]Sydney Institute for Astronomy, School of Physics, University of Sydney, New South Wales 2006, Australia. [4]Stellar Astrophysics Centre, Department of Physics and Astronomy, Aarhus University, Ny Munkegade 120, DK-8000 Aarhus C, Denmark. [5]Laboratoire Astrophysique Interactions Multi-échelles, Commissariat á l'Énergie Atomique/Direction des Sciences de la Matiére, CNRS, Université Paris Diderot, Institut de Recherches sur les lois Fondamentales de l'Univers/Service d'Astrophysique Centre de Saclay, 91191 Gif-sur-Yvette Cedex, France. [6]Department of Physics, University of California, Santa Barbara, CA 93106, USA.
***Corresponding author. E-mail: jfuller@caltech.edu (J.F.); matteo@kitp.ucsb.edu (M.C.)** †These authors contributed equally to this work.

Direct sampling of electric-field vacuum fluctuations

C. Riek, D. V. Seletskiy, A. S. Moskalenko, J. F. Schmidt, P. Krauspe, S. Eckart, S. Eggert, G. Burkard and A. Leitenstorfer

Science **350** (6259), 420-423.
DOI: 10.1126/science.aac9788originally published online October 1, 2015

Probing the fluctuating vacuum

According to quantum mechanics, a vacuum is not empty space. A consequence of the uncertainly principle is that particles or energy can come into existence for a fleeting moment. Such vacuum or quantum fluctuations are known to exist, but evidence for them has been indirect. Riek *et al.* present an ultrafast optical based technique that probes the vacuum fluctuation of electromagnetic radiation directly.

Science, this issue p. 420